

Cryogenic micro-calorimeters for mass spectrometric identification of neutral molecules and molecular fragments

O Novotný^{1,2}, S Allgeier³, C Enss³, A Fleischmann³, L Gamer³,
D Hengstler³, S Kempf³, C Krantz¹, A Pabinger³, C Pies³,
D W Savin², D Schwalm^{1,4}, A Wolf¹

¹ Max-Planck-Institut für Kernphysik, D-69117 Heidelberg, Germany

² Columbia Astrophysics Laboratory, Columbia University, New York, NY 10027, USA

³ Kirchhoff Institute for Physics, Heidelberg University, D-69120 Heidelberg, Germany

⁴ Faculty of Physics, Weizmann Institute of Science, Rehovot 76100, Israel

E-mail: oldrich.novotny@mpi-hd.mpg.de

28 November 2018; *Revision* : 1.12

Abstract. We have systematically investigated the energy resolution of a magnetic micro-calorimeter (MMC) for atomic and molecular projectiles at impact energies ranging from $E \approx 13$ to 150 keV. For atoms we obtained absolute energy resolutions down to $\Delta E \approx 120$ eV and relative energy resolutions down to $\Delta E/E \approx 10^{-3}$. We also studied in detail the MMC energy-response function to molecular projectiles of up to mass 56 u. We have demonstrated the capability of identifying neutral fragmentation products of these molecules by calorimetric mass spectrometry. We have modeled the MMC energy-response function for molecular projectiles and conclude that backscattering is the dominant source of the energy spread at the impact energies investigated. We have successfully demonstrated the use of a detector absorber coating to suppress such spreads. We briefly outline the use of MMC detectors in experiments on gas-phase collision reactions with neutral products. Our findings are of general interest for mass spectrometric techniques, particularly for those desiring to make neutral-particle mass measurements.

Keywords: mass spectrometry, calorimetry, micro-calorimeter, cryodetector, neutral reaction products

1. Mass spectrometry for multi-keV neutral particles

Mass spectrometry is one of the most important analytical techniques used in both fundamental sciences and industry applications. The diverse fields of use include protein and genome characterization in molecular biology [1, 2], determination of fundamental

constants [3], atmosphere composition characterization for Earth [4] and other solar system bodies [5], isotope dating [6], drug discovery [7], etc. Most molecular mass-spectrometry methods employ electromagnetic fields to determine mass-to-charge ratios of ionized particles [8]. Two major limitations arise from this approach. First, the mass-to-charge ratios may be ambiguous, e.g., singly charged monomers are indistinguishable from doubly charged dimers. Second, neutral fragments cannot be analyzed directly and a “neutral loss” must be accepted. To circumvent these limitations, the neutrals studied can be ionized and then analyzed in a standard way using electromagnetic fields [9]. Although “gentle” ionization methods exist nowadays (e.g., electrospray ionization [10]), the ionization often results in further fragmentation and in multiple ionization. Each of these processes can lead to a significant increase of complexity in the measured mass-to-charge spectrum [11]. Unfolding such data into a mass spectrum of the original sample may be complicated [12] and often only qualitative information can be retrieved [13].

Calorimetry represents an alternative approach to measure the masses of neutral particles. Calorimetric detection can be based on ionization, such as in the surface barrier or scintillation detectors applied mainly in nuclear and particle physics [14], or on thermal effects, as we discuss below. In all of these approaches, the calorimetric signal is proportional to the energy set free by the stopping of an incident particle, mostly given by its initial kinetic energy. Masses can be deduced from the magnitude of the kinetic energy if the incident velocity is known.

In molecular physics, calorimetric detection has been applied in particular to gas-phase collision studies using fast particle beams. For those studies many of the reaction products are neutral and their detection and mass measurement is essential in order to determine reaction cross sections and fragmentation branching ratios. A range of studies have been devoted to collision-induced dissociation (CID) of molecular and cluster ions in a fast beam, interacting with a stationary gas target (see, e.g., [15, 16] for recent work). Extensive work has also been directed to the study of dissociative recombination (DR) of molecular ions with electrons, which for singly charged ions produces exclusively neutral fragments [17]. DR is closely related to the process of electron capture dissociation (ECD), which is widely applied in the field of mass spectrometry for sequencing multiply-charged biomolecular cations [18, 19].

The DR reaction on singly charged ions was studied in particular with fast ion beams in a storage ring, utilizing a merged electron-ion beams configuration [20] where the electron-ion interaction energy could be tuned to small (sub-eV) values. Considering this reaction on a model molecule $ABCD^+$, the neutral fragmentation channels may include, e.g.,



In a fast ion beam, the parent ion velocity (corresponding to multi-keV or MeV ion beam

energies) is typically much larger than the relative velocities that the fragments gain in the dissociation process (from the typical kinetic energy release of $\lesssim 10$ eV). As a result, the DR products arising from the beam overlap region have velocities close to that of the parent ions. After separating the ion beam by means of magnetic or electrostatic fields the neutral DR products are collected by a kinetic-energy-sensitive detector. From the known parent ion velocity, and from the measured fragment kinetic energies, the fragment masses can in general be easily assigned. This method has been successfully used in combination with magnetic heavy ion storage rings [21, 22, 23, 24] operating at \sim MeV ion beam energies and utilizing surface-barrier detectors (SBDs) [25]. The approach, however, is restricted to high beam energies as SBD detectors have a thin, but significant, insensitive surface layer which cannot be penetrated by low-energy particles [26]. Moreover, even at MeV beam energies the energy resolution of SBDs is not sufficient to identify heavy neutral molecular fragments with 1 u resolution [27].

Stored ion beams of lower energy have been attracting significant attention for some time now [28]. One emphasis of these studies has been on complex molecular ions. In order to optimize the storage times of such ions and minimize the influence of thermal radiation, ion beam traps and storage rings involving cryogenic cooling of the enclosing experimental vacuum chamber have recently been commissioned or are currently under development. In these electrostatic storage devices [29, 30, 31, 32] the experimental vacuum chamber is cooled to ~ 10 K. The beam energy for stored singly charged ions typically ranges up to some $E \sim 30$ keV. Higher ion beam energies, up to 300 keV for singly charged ions, will be used in the cryogenic storage ring (CSR) [33, 34] at the Max-Planck-Institute for Nuclear Physics in Heidelberg, Germany. This ring is also being equipped for electron-ion merged beams experiments [34] to allow for DR experiments on complex molecular ions. It is this CSR development that mainly motivates the present search for alternative calorimetric detection techniques for molecular particles.

A promising approach for solving the needs for low kinetic energy measurements is the use of cryo-detectors [35], such as Superconducting Tunnel Junction detectors (STJ) or micro-calorimeters. In these detectors the incident particle excites various types of energy states in the absorbing bulk. Depending on the detector type, this excitation can be transformed into electrical signal. For example, in micro-calorimeters the particle kinetic energy is transformed into heat and a sensitive temperature monitoring then provides the measure of the kinetic energy deposited. For cryo-detectors, operation at low temperatures ($\lesssim 1$ K) is needed to limit thermal noise and thus resolve the measured low energies. The advantages of cryo-detectors were recognized as early as 1935 [36]. Their broader use was first motivated by astrophysical applications, e.g., in dark matter searches [37], and for high-precision X-ray spectroscopy [38].

In the 1990s the advantages of cryo-detectors were also recognized for classical mass spectrometry [39, 40]. Aside from the benefits explained above, an additional motivation for using cryo-detectors was their ability to resolve very slow massive molecules where standard microchannel plate detectors fail. Compared to microchannel plates, calorimetric detectors also offer a single-particle detection efficiency that could,

in principle, reach values very close to unity. On the other hand, the aspect ratio of the channels (typically about 0.7) limits the efficiency of microchannel plates for detecting single-particle impacts to significantly below unity for many applications. Various types of cryo-detectors have been implemented in previous mass spectrometric studies, mainly in time-of-flight mass spectrometry (TOF-MS) [40, 41, 42, 43]. Recently, and independently of our own attempts, a cryogenic STJ detector has been employed in a tandem mass spectrometer [44] following an approach similar to the calorimetric mass determination discussed above for gas-phase molecular collision and ion storage ring studies.

When used for X-ray spectroscopy [45] cryo-detectors can achieve an excellent relative energy resolution of $\Delta E/E \approx 10^{-4}$ and an absolute resolution down to $\Delta E \approx 1$ eV. For detecting massive particles, however, the resolution degrades by orders of magnitude. In heavy-ion experiments performed at MeV and GeV energy, resolutions of not better than $\sim 10^{-3}$ have been reached [46]. For α -spectrometry studies researchers measured $\Delta E/E \approx 5 \times 10^{-4}$ at $E = 5.5$ MeV [47, 48, 49]. However, energy resolutions of only $\sim 10^{-1}$ were reported for detecting atoms and molecules at energies of $\lesssim 10$ keV [40, 41, 42, 44, 50, 51], i.e., in the regime most relevant for mass spectrometry. Only a few studies have attempted to understand this issue. Andersen [52] theoretically predicted the cryogenic calorimeter energy resolution for heavy ions. In his calculations he included various projectile energy loss processes in the detector absorber, such as backscattering and Frenkel-pair formation, and estimated the amount of energy which is not converted into heat and thus cannot be detected. The statistical nature of the losses then defines the broadening in the acquired energy spectra. Quantitatively, Andersen's predictions for various detector types match to within an order of magnitude the energy resolutions measured later at MeV to GeV energies [46]. More recently Horansky et al. have numerically modeled the micro-calorimeter energy spectra from 5.5 MeV α -particles [47] and have concluded that the dominant spectral broadening is due to lattice damages. Their model underestimates the energy spread by a factor of ~ 2 compared to the measurements. We are not aware of any study attempting to theoretically describe the energy resolution of a cryo-detectors for massive particles at $E < 100$ keV energies. Similarly, to the best of our knowledge there are no systematic experimental studies of the energy resolution for cryo-detectors as a function of projectile energy and type for sub-MeV energies. In the energy range from ~ 10 keV to 5.5 MeV, even demonstration measurements are missing.

We therefore believe that the first step for understanding and eventually improving the cryo-detector energy resolution for mass spectrometry is a systematic study of the detector energy-response function for atomic and simple molecular projectiles at sub-MeV energies. To this end we have experimentally studied the energy resolution of a micro-calorimeter detector for atomic and molecular ions and neutrals at energies from ~ 13 to 150 keV. The rest of the paper is organized as follows: In Section 2 we briefly introduce the specific class of micro-calorimeters employed in our experiments, namely the metallic magnetic calorimeter (MMC). In Section 3 our experimental setup

is described. In Section 4 we present the acquired energy spectra and a corresponding model resolving the various energy loss processes. Based on this model, we also demonstrate the importance of detector absorber materials. We summarize and present our future plans in Section 5.

2. Metallic magnetic calorimeter (MMC) detectors

2.1. Detection principle

Micro-calorimeters are cryo-detectors typically operating at $\lesssim 100$ mK [35]. In this temperature regime the kinetic energy of a detected particle heats up the detector absorber such that the increase of the absorber temperature is proportional to the original projectile kinetic energy. The response is linear to a high degree. In order to monitor the absorber temperature, various sensor types can be used. MMCs are operated with paramagnetic sensors whose magnetization at low temperatures is a monotonic function of temperature. The magnetization change is measured with a superconducting coil inductively coupled to a superconducting quantum interference device (SQUID). A weak thermal link between the absorber and a cold thermal bath ensures that the absorber cools back to the bath temperature after the energy readout. A detailed description of the MMC operation principle and micro-fabrication can be found in [53, 54, 55].

2.2. Energy resolution

In general the energy resolution of an MMC detector setup is given by the thermal noise in the detector absorber and sensor, by the electronic noise in the signal processing system, and by the processes transforming the kinetic energy of the detected particle into absorbed heat. The thermal and electronic noise levels do not depend on the nature and energy of the detected particles and thus define the intrinsic energy resolution of the detector. For MMCs the intrinsic energy spread is typically $\lesssim 100$ eV (full width at half maximum, FWHM) and under very favourable conditions energy spreads of $\lesssim 1.6$ eV have been achieved [45, 56].

The kinetic energy transformation into heat is very efficient for X-rays. There the energy absorption process is dominated by the photoelectric effect, followed by the photoelectron efficiently heating the electron gas and subsequent energy transfer to the phonons [53]. Only a negligible part of the energy is lost, e.g., by kinetic energy of secondary electrons escaping the surface of the absorber. In contrast to detecting energetic photons, stopping atomic and molecular projectiles in the absorber may lead to additional processes, such as backscattering of the projectiles, sputtering of absorber material, and absorber lattice defect formation. All of these non-thermal processes remove part of the projectile kinetic energy before it can be converted into heat in the absorber and measured by the temperature sensor. Moreover, the statistical nature of these processes results in a spread of the detected energies. Thus in general the energy

resolution of an MMC detector (and cryo-detectors in general) depends on the absorber material as well as on the nature and energy of the impacting particles.

3. Experiment for determining MMC energy resolution

In order to experimentally determine the energy resolution of an MMC detector we have measured kinetic energies E_m of single ions from a nearly monoenergetic, mass-to-charge-selected ion beam. The accumulated single-particle calorimetric signals, after suitable calibration to yield E_m , were used to derive energy spectra $P_m(E_m, E_{ib}, M)$ which, in turn, were used to determine the corresponding energy resolutions. The measured spectra are labeled by the nominal ion beam energy E_{ib} and by the ion mass M (since the systems studied are simple enough to uniquely specify the ion type from its mass).

3.1. Ion beam production

Ion beams were generated using the high-voltage ion beam platform at the Max Planck Institute for Nuclear Physics in Heidelberg, Germany [34]. The various singly charged molecular cations were produced in a gas discharge from a Penning ion source. While still on the platform, they were accelerated in a first stage by ~ 13 kV and then filtered by their mass-to-charge ratio in a 90° dipole magnet. After passing through a set of apertures the ions were further accelerated in a second stage by the potential applied to the platform relative to ground. By adjusting the platform voltage, the final ion energies were varied in the range from $E_{ib} \approx 13$ to 150 keV. After leaving the platform the ion beam was focused and directed by an electrostatic quadrupole and a set of magnetic deflectors onto the detector setup ~ 10 m from the platform exit.

The nominal beam energy E_{ib} was determined as a sum of the two involved acceleration voltages used. The estimated systematic uncertainties in the E_{ib} scaling and offset are $\pm 0.5\%$ and ± 300 eV, respectively. Here and throughout all uncertainties are quoted at an estimated 1σ statistical confidence level.

Some of the tests turned out to be sensitive to instabilities in the acceleration voltages, resulting in a spread of individual ion energies E_i . We approximate the ion energy distribution $P_{ib}(E_i, E_{ib})$ by a symmetrical energy spread function peaking at E_{ib} with a FWHM of Δ_{ib} .

The voltage for the first-stage acceleration on the high-voltage platform was stable to within ≈ 5 V. For the second-stage acceleration by the high-voltage platform potential, two different voltage sources have been used. The first voltage source, hereafter denoted as A, was limited to 40 kV and was used for most measurements with $E_{ib} \lesssim 53$ keV. This source was stable to within ≈ 4 V. The spreads from the first- and second-stage acceleration, added in quadrature, result in a total ion energy spread of $\Delta_{ib}^A \approx 6$ eV. As will be shown in Section 4.1, this ion energy spread is negligibly small in comparison to the detector resolution.

For $E_{\text{ib}} > 53$ keV a less stable voltage source B was employed in the second-stage acceleration. The voltage fluctuations here dominate over those from the first-stage acceleration. Direct determination of the voltage spread was difficult and therefore we derived it from the difference in peak widths in the detected energy spectra P_{m}^{A} and P_{m}^{B} acquired with the same ion type, the same E_{ib} , but with voltage sources A and B, respectively. As shown below in Section 4.1, the spectra for atomic projectiles are dominated by a single Gaussian-like peak. Thus, by approximating $P_{\text{ib}}(E_{\text{i}}, E_{\text{ib}})$ with a normal distribution we estimated the ion beam energy spread for the voltage source B as

$$\Delta_{\text{ib}}^{\text{B}} \approx \sqrt{(\Delta_{\text{m}}^{\text{B}})^2 - (\Delta_{\text{m}}^{\text{A}})^2}, \quad (4)$$

where $\Delta_{\text{m}}^{\text{A}}$ and $\Delta_{\text{m}}^{\text{B}}$ are the FWHMs of P_{m}^{A} and P_{m}^{B} , respectively. We applied the procedure separately for the H^+ and Ar^+ data acquired at ~ 53 keV and obtained values of $\Delta_{\text{ib}}^{\text{B}}$ which are equal to within their statistical uncertainties. The error-weighted average of these two results is $\Delta_{\text{ib}}^{\text{B}} = 320$ eV. A conservative estimate of the total systematic error of this procedure is ± 100 eV, which exceeds the statistical error by a factor of ~ 2 . In Section 4.1 we discuss how we are able to improve our estimate for the systematic error.

3.2. Detector setup

The detector setup was developed at the Kirchhoff Institute for Physics of the University of Heidelberg, Germany. The MMC detector itself was derived from the well-established *maXs-200* design, which was originally developed for X-ray spectroscopy [57]. For the present measurements we have used only two detector pixels, each having a 0.45×2.0 mm² sensitive area. The absorber for one of the pixels was made of a 50 μm thick gold layer. If not explicitly mentioned otherwise, the data presented below have been obtained from this pixel. Selected measurements were performed with the second pixel where the 50 μm thick gold absorber was coated with an additional 180 nm thick layer of aluminum. In both cases incident atoms and molecules were stopped in the uppermost ~ 150 nm layer of material, as verified by calculations using the SRIM software (“Stopping and Range of Ions in Matter” [58]). Hence, the two detector pixels correspond to stopping in gold and in aluminum, respectively. The absorber itself has full contact to a 2.4 μm thick thermal sensor made of a dilute gold-erbium alloy, mixed at a mole fraction of $[\text{Er}]/[\text{Au}+\text{Er}]=885$ ppm. The erbium was depleted in ^{167}Er , which has a large hyperfine splitting and would otherwise add a large heat capacity at the operational temperature. A detailed description of the *maXs-200* microfabrication and performance has been given previously [57, 59].

The ~ 10 mK working temperature of our MMC detector was maintained with a dilution refrigerator. To minimize the heat flux from the 300 K black-body radiation of the ion beamline onto the detector, a set of radiation shields at 800 mK, 4 K, and 50 K surrounded the detector. Traveling along the ion beam trajectory, the beam encountered

a set of sequential ~ 1 cm apertures at 50 K followed by a single 4 K foil with ~ 4 μm -diameter pinholes to limit the radiation flux onto the detector head to below 1 nW. The pinholes were located so that there was at most one in front of each detector pixel. The pixel used in the analysis was selected by connecting the readout electronics described below. The rate of detected events was maximized before each data run by slightly steering the ion beam.

3.3. Data acquisition and processing

For each combination of ion species and ion beam energy we accumulated between 500 and 2000 detection events. For each event the electronic pulse from the thermal sensor was read out via the SQUID electronics, amplified, and digitized. The individual pulses were analyzed to derive the detected energies E_m and thus also the energy distribution $P_m(E_m, E_{ib}, M)$.

The electronic signal of the detector reflects the temperature of the magnetic moments of the paramagnetic sensor, which closely follows the absorber temperature. The temporal evolution of the signal is determined by the thermal links between the absorber, the sensor, and the thermal bath. In our setup a typical pulse reached its maximum amplitude within ~ 30 μs after the detection. The subsequent cooling results in an exponential signal decay with a time constant of ~ 5 ms. In our experiments the energies detected were small enough so that the sensor heat capacity can be approximated by a constant over the whole range of sensor temperatures occurring during the detection event. Additionally, the detector-operation temperature range was chosen so that the sensor magnetization was proportional to the sensor temperature. As a result, the shapes of the acquired electronic pulses were independent of the detected energy. Moreover, to a very good approximation the pulse amplitudes were linearly proportional to the heat released in the absorber. To obtain the detected energies on a relative scale we fitted the pulse amplitudes using a fixed pulse shape. Specifically we used the advanced fitting procedure based on optimal filtering, also called “matched filter” [60, 61].

To put the detected kinetic energies on an absolute scale we additionally detected photons from an ^{241}Am γ -source placed at ~ 15 cm distance from the detector. The photon energy from such a source peaks sharply at 59.5409 keV [62]. In our setup we have determined the γ energies with ~ 15 eV precision, which corresponds to $\sim 0.25\%$ uncertainty in the scale factor of the energy calibration. The non-linearity of the energy scale is expected to be less than 0.1% at 60 keV [63].

3.4. Detector energy-response function

The detector energy-response function relates the impacting ion kinetic energy E_i to the measured energy E_m . As explained in Section 2.2, the energy-response function of an MMC detector setup is determined by statistical processes. First, thermal processes in the absorber transform the kinetic energy E_i into heat E_h with a statistical distribution

$F_{\text{det}}^{\text{TP}}(E_{\text{h}}, E_{\text{i}}, M)$. This process may depend on the type of incident particles denoted by M . Second, the thermal noise in the detector and the various noises in the readout system convert E_{h} into the detected energy E_{m} . The response function corresponding to this second transform, $F_{\text{det}}^0(E_{\text{m}}, E_{\text{h}})$, reflects the intrinsic detector resolution. The overall detector response function is then a convolution of the two spreads in the E_{h} -domain:

$$F_{\text{det}}(E_{\text{m}}, E_{\text{i}}, M) = F_{\text{det}}^0(E_{\text{m}}, E_{\text{h}}) \otimes F_{\text{det}}^{\text{TP}}(E_{\text{h}}, E_{\text{i}}, M). \quad (5)$$

We show below that the detector energy-response function F_{det} can have a complex shape, but is still often dominated by only a single peak. When that is the case we can define the detector resolution $\Delta_{\text{det}}(E_{\text{i}}, M)$ as the FWHM of $F_{\text{det}}(E_{\text{m}})$ for a given E_{i} and projectile M . The relative resolution is then defined as $\Delta_{\text{det}}(E_{\text{i}}, M)/E_{\text{i}}$.

We have determined the intrinsic-resolution function of our detector setup, F_{det}^0 , by applying our standard event analysis procedure (as described above) on the time-dependent electronic signal acquired between the detection events. Fluctuations of this baseline signal arise from the same instabilities and noise sources in the detector and the data acquisition system that also act on the particle-generated pulses. As explained above, the detector signal scales linearly with the energy input. Thus the pulses derived from this baseline fluctuation reflect the intrinsic noise of the detection system and the distribution of their peak amplitudes can be used as a measure for the intrinsic energy resolution of our detector setup. The inferred F_{det}^0 displayed a Gaussian shape centered at 0 eV with a FWHM of $\Delta_{\text{det}}^0 = 107 \pm 5$ eV.

4. Results and discussion

We have acquired MMC energy spectra $P_{\text{m}}(E_{\text{m}})$ for various singly charged atomic and molecular ions in the energy range from $E_{\text{ib}} \approx 13$ to 150 keV. We first present our measurements with atomic ions in Section 4.1. In Section 4.2 we demonstrate the mass spectrometric capabilities of the MMC detector using molecular fragmentation measurements. In Section 4.3 we discuss the origins for the various features in the acquired spectra. The data in these first three subsections were collected using the uncoated gold absorber. In Section 4.4 we present the effects of the MMC absorber material on the shapes of the detected spectra. Then, in Section 4.5 we present exploratory observations revealing neutral fragmentation products from the acetone radical cation, the largest molecule studied here.

4.1. MMC detection of atomic ions

In Figure 1 we present four $P_{\text{m}}(E_{\text{m}}, E_{\text{ib}}, \text{H}^+)$ spectra acquired with proton beams at $E_{\text{ib}} = 14.7, 52.6, 89.9$, and 151.5 keV. In the figure we label the spectra as H_{a} , H_{b} , H_{c} , and H_{d} , respectively. Each spectrum is dominated by a sharp peak close to E_{ib} . A fit of the spectra in the vicinity of the peak using a Gaussian function gives FWHMs of

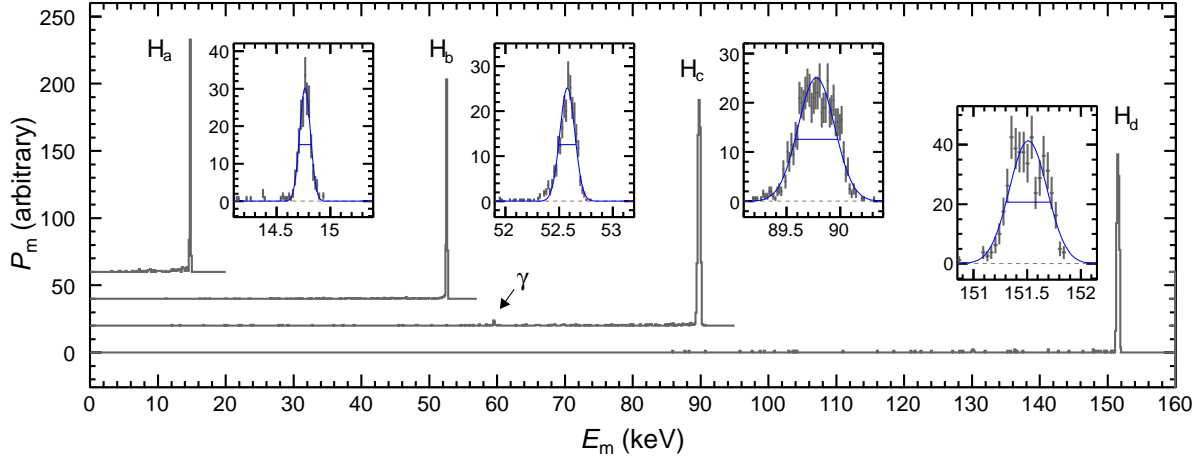


Figure 1. The MMC-detected energy spectra P_m for proton beams at $E_{ib} = 14.7, 52.6, 89.9$, and 151.5 keV are plotted in gray as a function of the detected energy E_m . We label the spectra as H_a, H_b, H_c , and H_d , respectively. The values of P_m are given on an arbitrary scale. In order to visually separate the spectra, vertical offsets have been added to H_a, H_b , and H_c . The γ -source signal is labeled in H_c . The insets display the spectral details close to the respective beam energies E_{ib} . The statistical error bars are displayed only in the insets. Gaussian-fit curves of the dominant peak in each spectrum are plotted in blue. The blue horizontal solid lines indicate the respective FWHMs and the dashed lines the baselines.

$\Delta_m = 117 \pm 7, 165 \pm 29, 401 \pm 10$, and 415 ± 26 eV. The errors given are the statistical uncertainties only.

Each of the acquired spectra is a convolution of the detector energy-response function and the ion energy distribution:

$$P_m(E_m, E_{ib}, M) = F_{\text{det}}(E_m, E_i, M) \otimes P_{ib}(E_i, E_{ib}). \quad (6)$$

For the H_a and H_b spectra, voltage source A has been employed to accelerate the proton beams. In this case, the ion energy distribution width Δ_{ib}^A , which has been determined independently (see Section 3.1), is negligibly small compared to the intrinsic detector resolution Δ_{det}^0 derived in Section 3.4. Hence, the ion beam energy distribution P_{ib} can be neglected in Equation (6). Correspondingly, the H_a and H_b spectra reflect directly the overall energy-response function F_{det} and the corresponding overall detector resolution is given by $\Delta_{\text{det}} = \Delta_m$. On the other hand for the spectra H_c and H_d , acquired with voltage source B, the widths of the prominent peaks are larger by a sizable factor, in spite of the only slightly higher ion energies. We conclude that the widths of these spectra are strongly influenced by the ion beam energy spread. From separate measurements (explained in Section 3.1) we derived a value of $\Delta_{ib}^B = 320 \pm 100$ eV for this energy spread. From the measured widths, and approximating both the measured spectra $P_m(E_m)$ and the ion energy distribution $P_{ib}(E_i)$ as normal distributions, we obtain the detector resolution as

$$\Delta_{\text{det}} \approx \sqrt{(\Delta_m)^2 - (\Delta_{ib}^B)^2}. \quad (7)$$

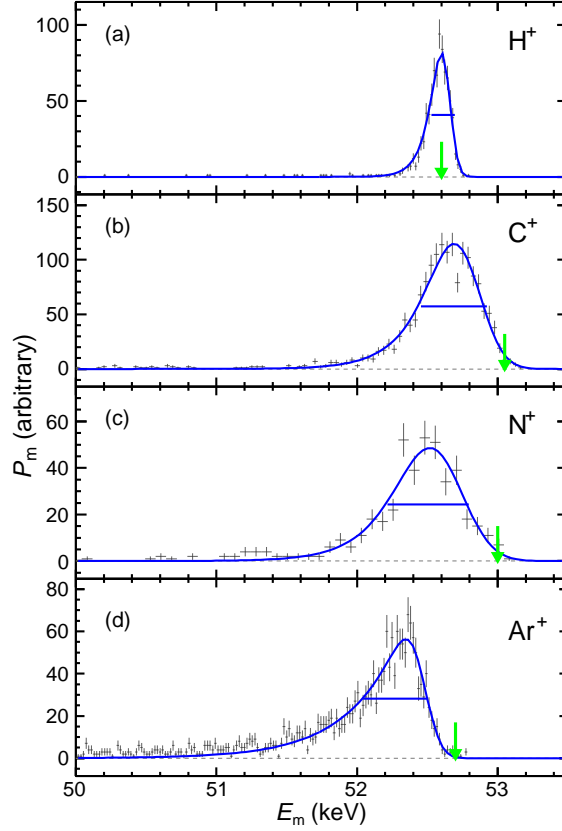


Figure 2. The MMC-detected energy spectra P_m for H^+ , C^+ , N^+ , and Ar^+ beams at beam energies around $E_{ib} = 53$ keV are shown by gray data points in panels (a) to (d), respectively. The data for H^+ and Ar^+ were acquired using voltage source A, while data for C^+ and N^+ were acquired using voltage source B. The statistical uncertainties are given by the vertical error bars. Green arrows mark the respective nominal ion beam energies E_{ib} . Fits by Equation (8) are shown by the blue curves. The blue horizontal lines indicate the respective FWHMs.

For the H_c and H_d spectra, we find $\Delta_{det} = 241 \pm 17$ eV and 264 ± 41 eV, respectively. The given errors reflect only the statistical uncertainties of the Δ_m widths. The inferred width Δ_{det} resulting from Equation (7) must be larger than the intrinsic detector resolution $\Delta_{det}^0 = 107$ eV. This requirement and the measured Δ_m for spectra H_c and H_d set an additional limit on the ion energy spread to be $\Delta_{ib}^B < 386$ eV. This enables us to reduce the estimated systematic uncertainty on the beam energy spread Δ_{ib}^B to $^{+66}_{-100}$ eV.

In addition to protons, we have studied the MMC resolution for the atomic ions C^+ , N^+ , and Ar^+ . In Figure 2 we compare the corresponding energy spectra $P_m(E_m)$ acquired at beam energies around $E_{ib} = 53$ keV. Similar to the proton spectra, the spectra of the heavier atomic ions are also dominated by a peak close to E_{ib} . In contrast, however, this main peak now has a clear tail extending towards low energies, suggesting that a small but significant part of the ion kinetic energy was not detected for a noticeable fraction of events with heavier atomic ions. In order to quantitatively

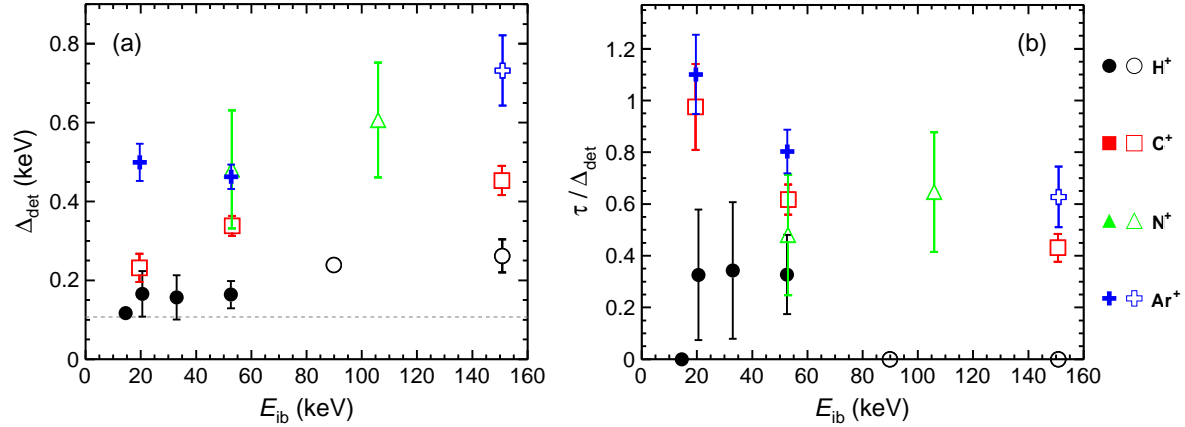


Figure 3. Panel (a): The widths Δ_{det} of the dominant peak feature in the MMC-detected energy spectra for various atomic ions are displayed as a function of the ion beam energy E_{ib} . The legend for ion types is displayed on the very right-hand side. The ion beams for the full-symbol data were accelerated by voltage source A. The correspondingly low ion energy spread was neglected. The hollow symbol data were acquired with a less stable beams using voltage source B. These widths were corrected for the ion energy spread using Equation (7). The error bars reflect the statistical uncertainties of the fitted widths, but do not include the $^{+66}_{-100}$ eV systematic error on the ion energy spread. The dashed line indicates the average intrinsic detector resolution of $\Delta_{\text{det}}^0 = 107$ eV. Panel (b): The peak asymmetry expressed as the ratio of the left-sided exponential decay parameter and the peak width (τ/Δ_{det}) is plotted as a function of E_{ib} . The meaning of the full/hollow symbols and of the error bars is identical to panel (a). The zero amplitude of some points (protons only) indicate fully symmetric peaks where the fit by Equation (8) failed for numerical reasons.

describe the resulting asymmetric peak shape we fit the spectra by a convolution of a Gaussian function and a left-sided exponential function [47, 64]

$$f(E_{\text{m}}) = \frac{A}{2\tau} \exp\left(\frac{E_{\text{m}} - E_0}{\tau} + \frac{\sigma^2}{2\tau^2}\right) \text{erfc}\left[\frac{1}{\sqrt{2}}\left(\frac{E_{\text{m}} - E_0}{\sigma} + \frac{\sigma}{\tau}\right)\right], \quad (8)$$

where A is the peak area, τ is the exponential decay parameter of the left-sided asymmetric part, E_0 is the peak position, σ is the Gaussian width, and erfc is the complementary error function. The fitting range was iteratively adjusted to $E_0 - 3\sigma - 3\tau \leq E_{\text{m}} \leq E_0 + 3\sigma$.

In Figure 3 we present the peak widths Δ_{det} and the asymmetry parameters τ/Δ_{det} for all of the atomic ion spectra. The measured width of each spectrum, Δ_{m} , is the numerically determined FWHM of the fitted function $f(E_{\text{m}})$. As explained above for protons, the detector resolution for measurements with voltage source A is taken as $\Delta_{\text{det}} = \Delta_{\text{m}}$. Similarly, we have corrected the widths Δ_{m} for spectra acquired with the voltage source B using the approximate method given by Equation (7).

The derived detector resolutions Δ_{det} for atomic ions, Figure 3(a), display a clear dependency on the ion type. The quantity Δ_{det} grows with increasing ion mass. The best MMC energy resolution was achieved for proton beams with $\Delta_{\text{det}} < 200$ eV at all measured values of E_{ib} . The narrowest spectrum was found with protons at

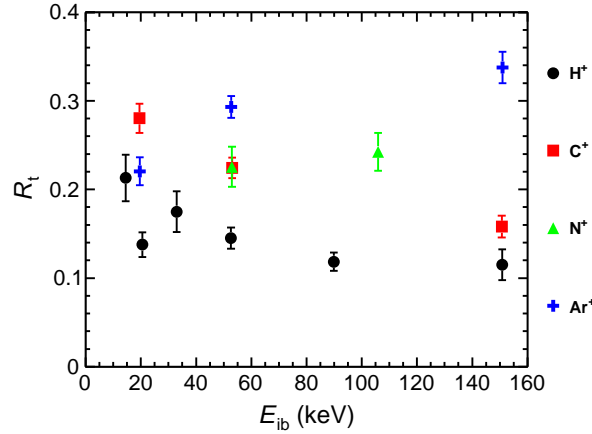


Figure 4. The fraction of events detected at energies below the dominant peak, R_t , is plotted as a function of ion beam energy E_{ib} for various atomic ion beams. The exact definition of the R_t fraction is given in the text. The error bars indicate statistical uncertainties.

$E_{ib} = 14.7$ keV, giving $\Delta_{det} = 117 \pm 7$ eV. The best relative resolution was achieved with protons at $E_{ib} = 151.5$ keV, namely $\Delta_{det}/E_{ib} \approx 1.7 \times 10^{-3}$. The peak widths increase for heavier atoms, reaching $\Delta_{det} \approx 700$ eV for Ar^+ . Given the large statistical uncertainties and the systematic uncertainty in Δ_{ib}^B (relevant for the hollow symbols), no clear dependency of Δ_{det} on E_{ib} can be identified.

In Figure 3(b) we show the peak asymmetry described by the ratio of the left-sided exponential decay constant τ to the peak FWHM (i.e., Δ_{det}). The most symmetric spectra - nearly Gaussian - were acquired with protons. Fitting these spectra using Equation (8) failed in some cases due to numerical divergence at $\tau \rightarrow 0$. In such cases we have used a pure Gaussian to fit the data and report a generic value for τ of “0”. Heavier atoms, compared to the protons, display more asymmetric peaks with a slightly decreasing tendency for increasing E_{ib} .

In all of the atomic ion measurements, most events were detected within the main peak, i.e., at energies of $E_0 - 3\sigma - 3\tau \leq E_m \leq E_0 + 3\sigma$. At higher energies no counts were recorded, which demonstrates the extremely low-background detection capability of MMC detectors. In the low-energy tails, the spectral count rates are small, decreasing smoothly towards lower energies (ignoring the events at ~ 59.5 keV from the γ source). In Figure 4 we plot the fractions of event counts detected in these far low-energy tails, defined as

$$R_t = \frac{\int_0^{E_0 - 3\tau - 3\sigma} P_m(E_m) dE_m}{\int_0^\infty P_m(E_m) dE_m}. \quad (9)$$

R_t reaches values as low as $\sim 10\%$ for high-energy proton projectiles. This fraction grows to up to $\sim 35\%$ for heavier atoms. For H^+ and C^+ a clear decrease of R_t with increasing E_{ib} can be seen. This trend cannot be seen in the N^+ data and even seems to be inverted for Ar^+ ions. Measurements presented in Section 4.4 show that the tail fraction is significantly reduced with the Al-coated absorber.

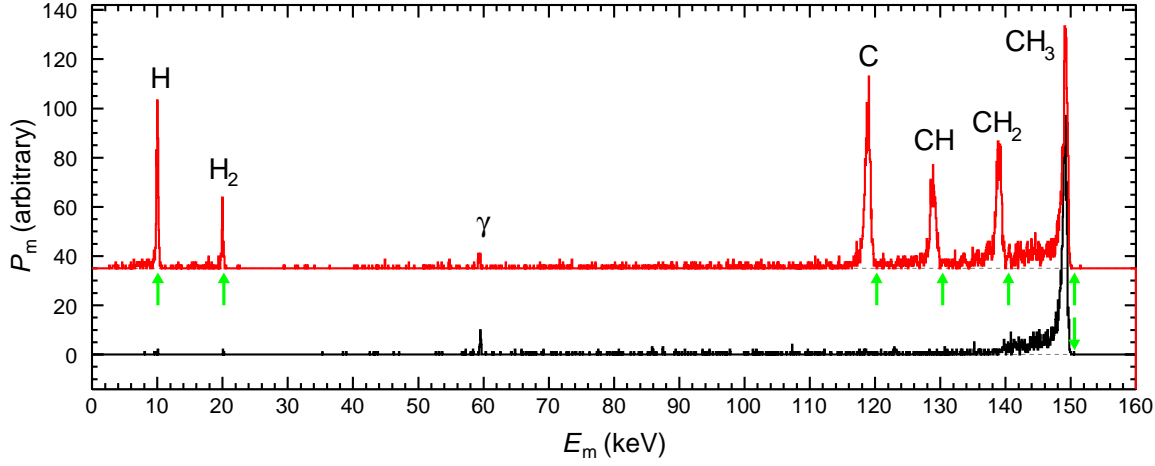


Figure 5. The MMC-detected energy spectra P_m for a CH_3^+ beam at $E_{\text{ib}} = 150.6$ keV is plotted by the black line as a function of the detected energy E_m . The red curve plots the spectrum acquired with ions prevented from reaching the detector, so that only neutral CH_3 and its neutral fragments were detected. The data have been vertically shifted from zero in order to visually separate the two spectra. The rightmost green arrow indicates the nominal ion beam energy E_{ib} and the remaining green arrows, going from left to right, show the energy fraction corresponding to the masses of H, H_2 , C, CH, and CH_2 fragments.

4.2. MMC mass spectrometry on molecular ions

In addition to atomic ions we have also studied the calorimetric detection for several types of molecular ions. As an example we plot the detected energy spectrum for a beam of CH_3^+ at $E_{\text{ib}} = 150.6$ keV in Figure 5 (black line). Similar what we found for atoms, this molecular spectrum is dominated by a single peak near to E_{ib} . From the peak width of $\Delta_m = 786 \pm 71$ eV and from the ion beam energy spread Δ_{ib}^B , we derive a FWHM detector resolution of $\Delta_{\text{det}} = 718 \pm 78$ eV. This exceeds the energy width for C^+ atomic ions (Figure 3) by ~ 200 eV.

Using an energetic molecular ion beam allowed us to demonstrate the MMC mass spectrometry capabilities directly in a single measurement. For this we directed all of the charged particles away from the detector, using a magnetic deflector placed ~ 1 m upstream of the detector. In this configuration, the only remaining particles hitting the detector were neutral atoms and molecules resulting from collisions of the molecular ions with residual gas in the ion beam line. Clearly, only a small fraction of the collision-induced neutrals are able to reach the MMC detector through the narrow pinhole in the mask in front of the detector. Thus, to reach acceptable data quality from this measurement configuration we have used high ion beam intensities and increased residual gas pressure in the beamline. Processes leading to neutral fragments are discussed in Section 4.5.

The red curve in Figure 5 displays the energy spectrum of neutral fragments resulting from collisions of CH_3^+ ions at $E_{\text{ib}} = 150.6$ keV with residual gas molecules

along the upstream beam line and reaching the detector pixel through the pinhole mask. The spectrum displays distinct peaks at energies matching well to the respective fragment-to-parent mass fractions of E_{ib} for all possible fragments of the CH_3^+ . The peak widths in the neutral spectrum are $\Delta_m = 333 \pm 20$ eV for H, 349 ± 46 eV for H_2 , 908 ± 180 eV for C, 1230 ± 67 eV for CH, 1013 ± 155 eV for CH_2 , and 813 ± 78 eV for CH_3 . The CH_3 peak width is equal to that from the CH_3^+ spectrum (to within the statistical uncertainty). This suggests that the molecular velocity is not significantly altered in the non-dissociative neutralizing collision with the residual gas. Moreover, this also allows us to conclude that the charge of the detected particle is irrelevant for the calorimetric measurement, to within the detector resolution.

Interestingly, the peaks for the CH and CH_2 fragments are clearly broader than that for CH_3 . The additional spread may originate from the kinetic energy released in the CH_3 dissociation process. For example, for a 150 keV CH_3 beam, a center-of-mass kinetic energy of 1 eV released into CH and H_2 fragments dissociating along the ion beam axis transforms into an ~ 260 eV change of the fragment kinetic energy in the laboratory frame. Since the present measurements detect only a small fraction of the neutral fragments produced in the beam, the relative detection yields for the different fragment species may depend significantly on the energy released and the angular emission pattern of the respective fragmentation channels. Nevertheless, we find that even under these non-ideal conditions the high-resolution calorimetric mass spectra still yield qualitative information about the molecular composition and the fragmentation channels.

In a more pronounced fashion than for the atoms, the mass peaks for both the primary molecular ion and the neutral molecular fragments are accompanied by tails that will be further discussed below. These wider tails turn out to be significantly influenced by the coating of the absorber in which the molecular stopping occurs (see Section 4.4).

4.3. Modeling MMC energy spectra

As was shown above (Section 4.1), the detected energy spectra for atomic projectiles are dominated by a single narrow peak close to the nominal ion beam energy E_{ib} , while more complex shapes are found for molecular projectiles. Thus, the CH_3^+ data at $E_{ib} = 150.6$ keV (Figure 5, black line) display a low-energy shoulder on the main peak in the energy range from ~ 140 to 147 keV. We find that the relative intensity of this feature grows significantly for lower ion beam energies, as seen in the CH_3^+ data acquired at $E_{ib} = 53.3$ keV (Figure 6). Similarly, we also observed prominent low energy shoulders in energy spectra recorded for CO_2^+ and $(\text{CH}_3)_2\text{CO}^+$ beams.

In order to understand the detected spectral shapes we have modeled the processes occurring during the stopping of molecular projectiles in the MMC absorber. In our simplified model we assume that the detected molecule breaks into separate atoms immediately after impinging on the detector surface and neglect the few eV of molecular binding energy. Additionally, we disregard the charge state of the projectile particles,

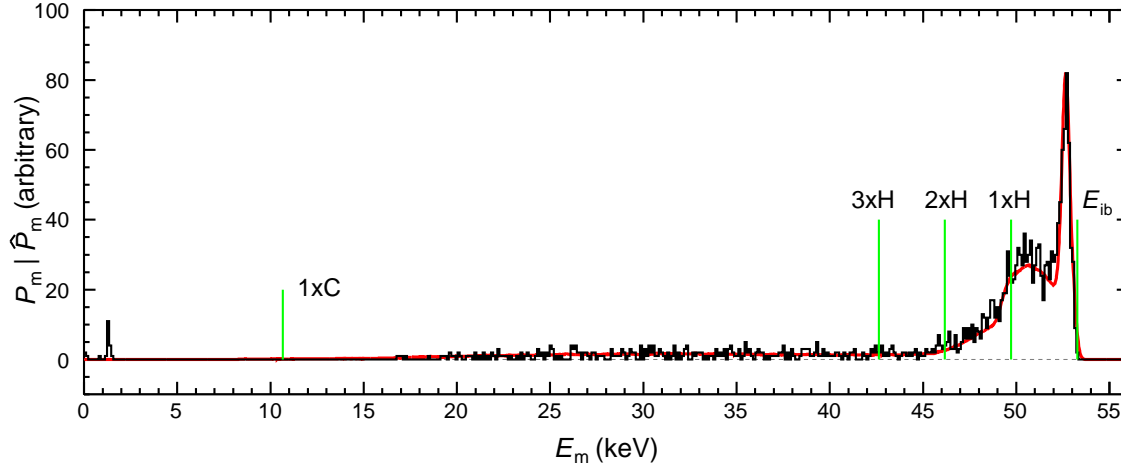


Figure 6. The MMC-detected energy spectra P_m for CH_3^+ beam at $E_{ib} = 53.3$ keV is plotted by the black line as a function of detected energy E_m . The red curve represents our SRIM-based model spectrum \hat{P}_m , assuming a Frenkel-pair energy $E_{FP} = 2.8$ eV. Going from right to left, the green vertical lines mark the nominal ion beam energy E_{ib} and the maximal energy losses due to backscattering of one, two, and three H-atoms, and one C-atom. The model spectrum is scaled in amplitude so that the integral between $E_m = 5$ keV and 54 keV matches the experimental data.

based on our findings described earlier. With these assumptions we can study stopping processes in the absorber separately for each of the atomic constituents of a given molecule, such as C and H in case of CH_3^+ . The model for the molecular spectra can then be constructed from a suitable combination of the modeled atomic spectra.

We have employed the SRIM software to simulate the energy loss processes of the projectile atoms in the MMC absorber. SRIM [58] is a 3D Monte-Carlo code that simulates the propagation of ions in matter. It describes not only collisions between the projectile and target atoms, but also accounts for target-target collisions due to cascades triggered by recoiling target atoms, backscattering of projectiles, and sputtering of atoms from the target material. The resulting detailed data on each collision allows us to evaluate the amount of projectile kinetic energy which is not transformed into heat and thus escapes calorimetric detection. Specifically, for each simulated detection event we have calculated whether the projectile atom was back-scattered, and if yes, then what fraction of the kinetic energy has remained in the absorber. Next, we have evaluated the number and the total kinetic energy of target atoms sputtered from the detector surface. Lastly, for each impact we track the number of defects created in the absorber lattice. Such defects arise when an atom of the target lattice is kicked out by recoil from its stable position (either by the projectile atom or another recoiled target atom). The resulting pair of an interstitial atom and a vacancy in the lattice (i.e., a Frenkel pair or a Frenkel defect [65]) holds a potential energy E_{FP} . This non-thermal energy storage results in a reduction of the energy detectable by the MMC. The SRIM code calculates the number of Frenkel defects along each incident ion track. To obtain the total energy loss due to Frenkel pair formation we multiply the number of Frenkel

pairs by E_{FP} which is a parameter of our model. The number of replacements where an energetic target atom terminates its movement in a previously created vacancy, is negligible. Altogether, for each impact event we have subtracted the above listed energy losses from the initial kinetic energy of the incident atom and thus obtain individual atomic detected energies $E_{\text{m}}^{\text{ato}}$. For a given molecule, we simulate 10^4 impact events related to each atomic constituent type. This yields the model energy spectra for each atomic species.

An additional loss of energy may arise from secondary electron emission by the detector absorber after the impact of a particle. Studies on secondary electron emission from solid gold targets, however, have found only small secondary electron yields of $\lesssim 2$ electrons per incident ion [66, 67] and mean secondary electron energies of ~ 10 eV [68] for a broad range of projectile energies and projectile types. Based on those studies we estimate the energy loss due to secondary electron emission to be negligible compared to the other energy loss processes and we do not include it in our model.

To calculate the detectable energy for a molecular projectile, $E_{\text{m}}^{\text{mol}}$, we have randomly picked simulated events for each of the constituent atoms and sum the corresponding $E_{\text{m}}^{\text{ato}}$ values. Then we have added a random Gaussian spread describing the intrinsic detector resolution ($\Delta_{\text{det}}^0 = 107$ eV) and the ion energy spread ($\Delta_{\text{ib}}^{\text{B}} = 320$ eV FWHM), obtaining the model energy distribution $\hat{P}_{\text{m}}(E_{\text{m}})$. Adding the ion beam energy spread only in the last step (instead of varying E_{i} as the input parameter of the SRIM simulations) is justified by the small relative ion beam energy spread of $\Delta_{\text{ib}}^{\text{B}}/E_{\text{ib}} < 1\%$, within which the relative contributions of the various energy loss processes stay nearly constant.

In Figures 6 and 7 we compare the model energy distribution \hat{P}_{m} for CH_3^+ at $E_{\text{ib}} = 53.3$ keV to the corresponding experimental data. In red we plot the result of the complete model including all of the energy loss processes mentioned above and for the value of E_{FP} yielding the best agreement with the data. Partial effects are shown in Figure 7 for the Frenkel-pairs only (blue) as well as for Frenkel pairs plus sputtering (green). Comparing this latter curve with the full result (red) shows the rather strong effect of the backscattering process. The curves for the Frenkel-defects only are also shown for a range of E_{FP} values.

The shape of the dominant peak at $E_{\text{m}} = 52.7 \pm 0.5$ keV can be assigned to the energy spread due to Frenkel pair formation. The Frenkel-pair energy used in the model affects only this feature in its width and mean energy. Comparing directly the peak energy in the model to the measured data is difficult due to the systematic uncertainty in the nominal ion beam energy E_{ib} (Sec. 3.1). Instead we have varied the E_{FP} value in steps of 0.05 eV and in each iteration compared the width of the dominant peak in the model spectra to that in the measured data. Simultaneously we adjusted the model beam energy so that the center of the peaks overlap. The best match was reached for $E_{\text{FP}} = 2.8$ eV and by adjusting the model beam energy by +0.1 keV (this is only 0.2% of E_{ib}) with respect to the nominal beam energy of $E_{\text{ib}} = 53.3$ keV. Such an energy shift is well below the estimated E_{ib} uncertainty. The energy losses due to sputtering of

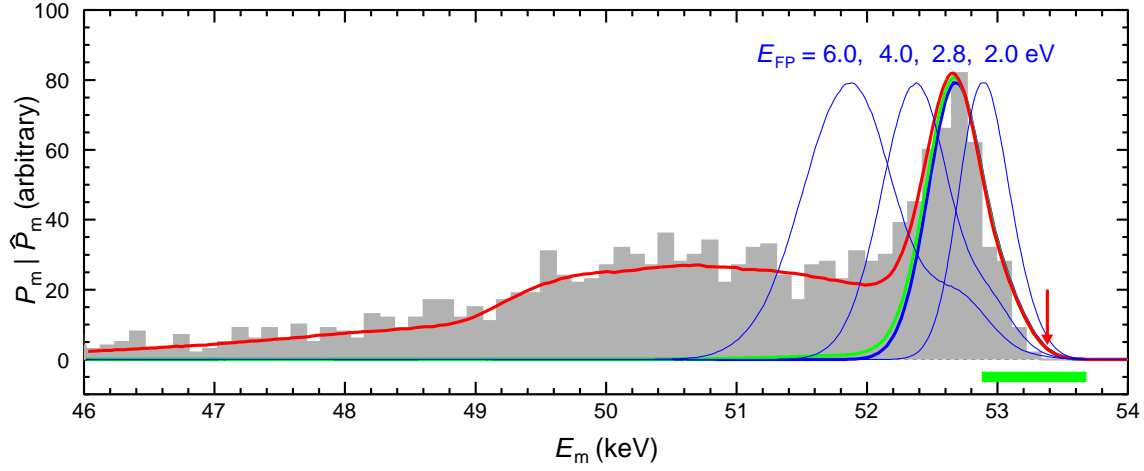


Figure 7. A comparison of the MMC detected energy spectrum (gray) and a corresponding SRIM-based model for CH_3^+ (red). The thick blue line plots the model spectrum assuming energy losses only via Frenkel-pair formation with an adjusted Frenkel-pair energy of $E_{\text{FP}} = 2.8$ eV. The thin blue lines plot the same model using an alternative value for E_{FP} of 6.0 eV, 4.0 eV, and 2.0 eV, respectively. The green line plots the model assuming Frenkel-pair formation and sputtering. The difference between red and green line then reflects the effect of backscattering. The horizontal green bar labels the uncertainty range for the nominal ion beam energy $E_{\text{ib}} = 53.3 \pm 0.4$ keV in the experiment. The red arrow marks the adjusted ion beam energy for the model.

absorber atoms add only a small left-handed tail on the main peak and do not produce any distinct spectral feature. Backscattering of H atoms is responsible for the wider feature between ~ 45 and 52 keV and backscattering of C for the tail remaining visible down to ~ 15 keV. The small feature at ~ 1.2 keV was not observed in most of other acquired spectra and is interpreted as a spurious event not originating from CH_3^+ .

Backscattering appears to be the key for explaining the differences between the atomic and molecular spectral shapes beyond the main peak. For atomic projectiles, the observed low-amplitude and low-energy tails are attributed to backscattering of the projectile atoms themselves; any of the back-scattered atoms can take away up to the full original kinetic energy. Typical spectra can be seen in Figure 1. On the other hand, for molecular projectiles the dissociated atomic fragments are expected to backscatter independently, each fragment being able to carry away only the part of the original projectile kinetic energy given by the fragment-to-molecule mass ratio. In the case of CH_3^+ , energy loss maxima of $E_{\text{ib}}/15$ and of $12E_{\text{ib}}/15$ result for backscattered single H and C atoms, respectively. Given the H multiplicity, the most likely backscattering process is that of a single H fragment, taking away energy between 0 and $\sim E_{\text{ib}}/15$. As a consequence we observe a strong, broad feature in P_m between $E_m \approx E_{\text{ib}} - E_{\text{ib}}/15$ and $E_m \approx E_{\text{ib}}$. Structures in P_m at lower energies decrease in magnitude as the simultaneous backscattering of multiple H atoms becomes less probable. The lowest energies can be accessed only by backscattering of carbon atoms.

Only a few parameters enter our model. The most influential one is the Frenkel-pair

energy which directly scales the width and position of the main peak. Our fitted value $E_{\text{FP}} = 2.8$ eV has a strong correlation with the beam energy spread $\Delta_{\text{ib}}^{\text{B}}$. The $^{+66}_{-100}$ eV uncertainty of $\Delta_{\text{ib}}^{\text{B}}$ causes an uncertainty of $^{+0.9}_{-0.6}$ eV in the adjusted value of E_{FP} .

Another important parameter entering the SRIM model is the threshold displacement energy E_{displ} , i.e., the minimum energy needed for a recoiling target atom to overcome the lattice barrier, move away from its original position, and form an interstitial. In our model we use $E_{\text{displ}} = 43$ eV, a value recommended in a recent review [69]. The E_{displ} values listed in that review range from 30 eV to 44 eV. Using this range as the uncertainty in E_{displ} results in an uncertainty of $^{+0.1}_{-0.7}$ eV for E_{FP} .

Furthermore we set the lattice binding energy to $E_{\text{latt}} = 3.81$ eV [65] and the surface binding energy for gold to $E_{\text{surf}} = 3.83$ eV [70]. In the SRIM simulation E_{latt} is the energy that every recoiling target atoms loses when it leaves its lattice site. E_{surf} is relevant for calculating sputtering. The estimated 0.5 eV uncertainties on E_{latt} and E_{surf} propagate to a negligible uncertainty in E_{FP} . For details on the relations between E_{displ} , E_{latt} , and E_{FP} see, e.g., the SRIM documentation [58] or Figure 11 in [47].

Adding all the systematic uncertainties together in quadrature gives a Frenkel-pair energy of $E_{\text{FP}} = 2.8 \pm 0.9$ eV. To the best of our knowledge, no other experimental values of E_{FP} have been published for gold. Calculated values range from $E_{\text{FP}} = 3.0$ to 4.1 eV, depending on the calculational method as well as on the specific lattice defect type formed [71, 72]. The Frenkel-pair energy determined from our model matches well with these calculated values.

4.4. Optimizing MMC resolution - absorber materials

Practical usage of the MMC detector for spectrometry requires a narrow energy-response function. We have shown that the dominant peak in all of the collected energy spectra is narrow and that relative resolutions down to $\sim 10^{-3}$ can be reached. Nevertheless, the low-energy tails of the energy-response function can significantly complicate the analysis of energy spectra, especially for molecular projectiles.

Our modeling studies indicates that the low-energy tails in the measured spectra originate predominantly from backscattering. Thus, in order to optimize the MMC energy-response function, we have searched for absorber materials with low backscattering probabilities. SRIM models show a general trend of lower backscattering for materials composed of lighter atoms (i.e., lower atomic number Z). Backscattering is determined predominantly by the first few surface monolayers. Hence only a thin absorber coating of a low- Z material should be sufficient to improve the MMC energy-response function. Moreover, SRIM calculations indicate that fewer Frenkel pairs should be created in low- Z materials. Thus, provided that the Frenkel-pair energy does not depend on the absorber material or is lower for a specific low- Z material, then the dominant peak should also narrow.

To test this hypothesis we have coated the 50 μm gold absorber of one of the MMC pixels with 180 nm of aluminum. In Figure 8 we compare the energy spectra from the

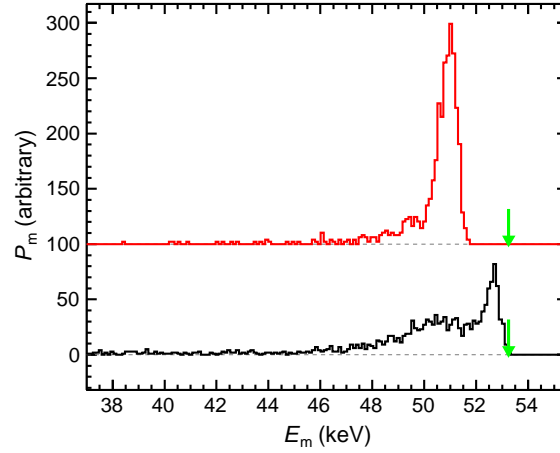


Figure 8. MMC detected energy spectra for CH_3^+ at $E_{\text{ib}} = 53.3$ keV, acquired with the gold-absorber pixel (black) and with the aluminum-coated pixel (red). The amplitude of the spectra have been scaled such that the total integrals are equal. An artificial offset in P_m has been added for clarity. The green arrows label the nominal ion beam energy E_{ib} .

bare and Al-coated gold pixels, acquired with the same beam of CH_3^+ at $E_{\text{ib}} = 53.3$ keV. Clearly, using an Al coating results in a strong suppression of the backscattering. There is a clear reduction near 50 keV in the shoulder due to backscattering of H atoms, and also a clear decrease below 46 keV in the tail due to backscattering of C atoms. Interestingly, the main peak is shifted towards lower energies when using the Al-coated absorber. This cannot be reproduced by our SRIM-based model. We anticipate that the shift is due to the aluminum being superconductive at the MMC operating temperatures, which is below the aluminum critical temperature of $T_c = 1.2$ K. Hence, the energy loss processes in the Al-coated pixel may be different from those for normal-conducting gold. This interpretation is supported by previously published experiments investigating the properties of various superconductors when used as a particle or X-ray absorber in a micro-calorimeter. At first glance, superconductors seem to be a very promising class of cryodetector materials, considering their relatively small specific heat at temperatures well below T_c . However, as shown by [73], which summarized earlier work on various superconductors, and by more recent studies [74, 75, 76] on aluminum and rhenium, the thermalization of energy in superconductors is not well understood at temperatures as low as that of our absorber at ~ 10 mK. At these temperatures there is very little phonon excitation ($T \lesssim 2 \times 10^{-4} \Theta_D$, where Θ_D is the Debye temperature) and surprisingly long thermal pulse decay times have been observed [74]. Analysis of these measurements suggests that a significant fraction of the deposited energy, from a few percent to tens of percent, could be stored in very long-lived excitations with lifetimes ranging up to several seconds. This fraction of energy would escape detection. The relevant long-lived excitations could be due to quasi-particles resulting from broken Cooper pairs, excitations of magnetic flux lines, or excitations of nuclear spins or atomic tunneling

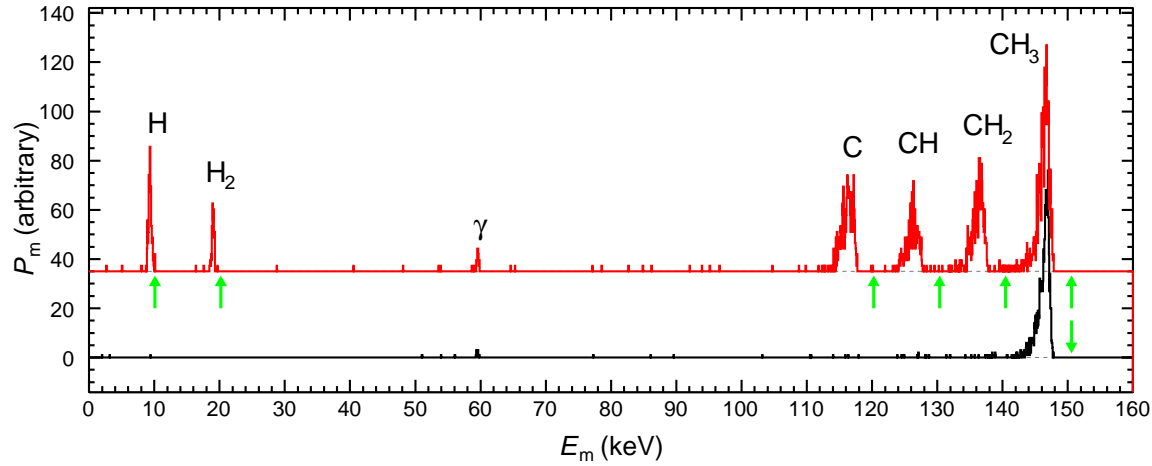


Figure 9. Same as Figure 5, but acquired with the Al-coated MMC absorber.

systems, to name just a few possibilities. In fact, the apparent magnitude of the energy loss in our detector with the aluminum coating, on the order of 5%, fits well to these previous observations and interpretations.

We also used the Al-coated detector pixel to reproduce the measurements on neutral CH_3^+ fragments created by residual gas collisions of CH_3^+ ions at $E_{\text{ib}} = 150.6$ keV (see Section 4.2). The results are displayed in Figure 9. A comparison to the data acquired with the bare gold absorber (Figure 5) shows, again, a strong reduction of the low-energy tail when the Al-coated absorber is used.

4.5. Acetone radical fragmentation

Using our MMC setup we have also investigated the fragmentation of acetone radical cations, $(\text{CH}_3)_2\text{CO}^+$ (58 u), due to residual gas collisions. To detect the neutral fragments we followed the approach outlined in Section 4.2. The data acquired at $E_{\text{ib}} = 150.45$ keV using the Al-coated detector pixel are displayed in Figure 10. Similar to our other measurements with this pixel, the measured energies are $\sim 4\%$ lower than those obtained with the gold-only pixel. For this large molecule, the data obtained with the uncoated gold pixel (not shown here) are much less resolved than those from the Al-coated pixel, although, as was consistently seen, the full-mass peak for the uncoated pixel lies much closer to E_{ib} . In the neutral fragment spectrum of Figure 10 (collected using the Al-coated pixel) we assigned the most distinct peaks by multiplying the fragment-to-molecule mass ratios by a full kinetic energy of only 96% of E_{ib} (the energy step corresponding to 1 u is then 2.49 keV). The small shifts between the peak centers and the predicted fragment energies, seen for only a few specific fragment masses (notably near 13 u at ~ 32 keV), may be due to more complex, still unexplained effects in the stopping of the molecular species.

Two processes are expected to generate the neutral fragments. The first is collision induced dissociation (CID, also known as collision activated dissociation - CAD), which

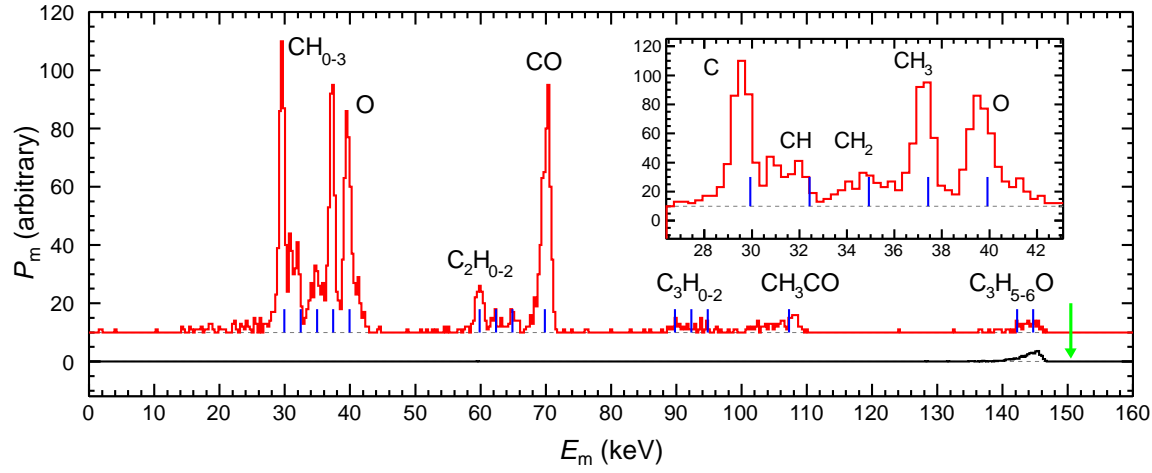
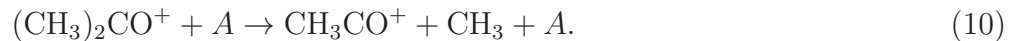


Figure 10. Same as Figure 5, but for acetone radical ions $(\text{CH}_3)_2\text{CO}^+$ at $E_{\text{ib}} = 150.45$ keV (black line) and for neutral products from colliding these ions with residual gas (red curve). In both cases the Al-coated MMC absorber was used. The blue vertical lines mark the expected energies of the various neutral fragmentation products (see the text for a detailed explanation). The green arrow indicates the nominal ion beam energy E_{ib} .

does not change the charge of the target particle (a residual gas molecule in our case). In CID at least one of the projectile fragments stays charged. The second process is an electron transfer from the neutral target to the projectile cation neutralizing it. As in electron-ion recombination, the ionization energy released then usually leads to the dissociation of the neutralized projectile molecule into neutral fragments (known as electron transfer dissociation - ETD). The electron transfer may also result in an internally excited, but non-dissociated, neutral molecule.

We also want to emphasize here that the setup used in these exploratory studies was not designed for quantitative branching ratio measurements. The kinetic energy released in the various CID and ETD outgoing channels may vary significantly. This affects the transverse distribution of the fragment impact positions on the detector. As a result, the true geometrical efficiency for detecting the fragments through the pinhole in front of the detector may vary strongly as well. Thus, the relative peak heights should be interpreted with care. Nevertheless, we find that the high mass resolution of our setup provides unprecedented insight in the CID and ETD channels producing neutral fragments by showing a number of discrete fragment mass peaks.

Many studies exist on CID and ETD of the acetone radical [77, 78, 79, 80, 81]. However, the vast majority of the techniques used collected only charged reaction products. Given this limitation, these studies assigned the dominant dissociation channel to



Here A is the target particle, which in our case of a non-baked UHV beam line is expected to be H_2O , N_2 , CO , or H_2 [82]. We are aware of only one study on acetone

radical fragmentation capable of also collecting neutral fragments. In specific, Ohkubo et al. [44] used a cryogenic STJ detector in a novel mass spectrometry approach for their investigations of 3 keV acetone radicals colliding with Xe atoms. They explained their data by two additional ETD channels producing solely neutral fragments:



However, their relative resolution of only $\Delta E/E \approx 0.14$ was not sufficient to resolve molecular fragments differing only by the number of attached hydrogen atoms.

Our results clearly show neutral fragments which do not originate from any of channels (10) – (12). The most interesting aspect of our data indicates that there is significant production of single C and O atoms as well as of the non-hydrogenated carbon molecules C_2 and C_3 . In the measurements of Ohkubo et al., due to their lower relative energy resolution, any potential contribution from these fragments would be hidden in the peaks assigned as CH_3 , CO , or CH_3CO . A full comparison between their work and ours certainly needs to take into account the differences between the two studies including collision energy, target gas, and probably also internal excitation of the projectile ions. Nevertheless, the various neutral fragmentation channels are more clearly resolved in the present results. This demonstrates the wealth of new information accessible by calorimetric detection of molecular fragments with high relative energy resolution.

5. Summary and Outlook

We have studied the energy resolution function of an MMC detector for kinetic energy measurements of atomic and molecular projectiles in the energy range from ~ 13 to 150 keV. For atomic projectiles we have demonstrated that relative resolutions down to $\Delta E/E \sim 10^{-3}$ can be achieved. For C and H, the most relevant atomic projectiles in organic chemistry, relative resolutions below 10^{-2} were reached at all projectile energies studied. Additionally, we have studied the response of the MMC to molecular projectiles and demonstrated the capability of calorimetric mass spectrometry to identify molecular fragmentation products.

We have also created a model of the micro-calorimeter energy resolution for molecular projectiles. The model was used to fit experimental data from CH_3^+ and a very good qualitative and quantitative reproduction of the measured spectra was found. The quality of the model allowed us to resolve the contributions of the various energy-loss processes to the detector energy-response function. For molecules, the dominant distortion of the spectra originates from energy loss due to backscattering. Based on this finding we have experimentally demonstrated the strong influence of the absorber material on the detector energy-response function. Specifically, using a thin aluminum coating on the absorber resulted in a strong reduction of the distortion from backscattering. The validity of our model has been demonstrated for an MMC detector.

Nevertheless, similar energy-loss processes are expected to occur in all types of cryo-detectors, including other micro-calorimeter types and STJs. Thus our findings on the MMC energy-response function are likely to be relevant for cryo-detectors in general.

To the best of our knowledge, our work is the first experimental study of the energy-response function of cryo-calorimeter detectors for atomic and molecular projectiles over the energy range covered. This model, which we have developed to estimate the energy-response function, can be used by us and by others to extrapolate our findings to lower projectile energies and more complex molecular projectiles. In future studies we will investigate other coating materials in order to further improve the detector energy-response function.

Implementation of micro-calorimeter detectors for fragmentation studies, such as the DR measurements at CSR proposed in Section 1, requires not only a high energy resolution, but also a large sensitive area, coincident fragment detection capability, and position resolution. To meet these requirements we have taken two different segmented MMC-design approaches. Segmentation provides the ability to detect coincident particles. The first approach consists of using large-area detector segments operated independently. Using a special configuration of thermal links between the absorber, sensor, and heat bath allows one to determine the incident position within each segment. This configuration has been realized and successfully tested on a circular prototype detector of 34 mm in diameter with 16 pie-like segments [83, 84]. The second approach involves our development of a large 4 kilo-pixel MMC detector with an active area of $44.8 \times 44.8 \text{ mm}^2$. The 64×64 particle absorbing pixels making up this detector are coupled to a square array of paramagnetic temperature sensors. The sensor pickup coils are wired to provide for each row and each column of this array a summed temperature signal from all of the sensors in the respective row or column. This approach reduces the number of readout channels from $O(N^2)$ to $O(2N)$, where N is the dimension of the square detector. Compared to the first approach, this pixelized detector will have a more uniform spatial resolution and higher multi-hit capability [85].

Based on the results of our present MMC energy-response study and of the large-area position-sensitive MMC developments, briefly described above, we conclude that MMC detectors are now a realistic option for applications in atomic and molecular collision experiments and in mass spectrometry at keV energies. Our priority is to implement such a large detector in the recently commissioned electrostatic Cryogenic Storage Ring (CSR) at the Max Planck Institute for Nuclear Physics in Heidelberg, Germany [33, 34]. The system will be used for electron-ion merged-beams studies as explained in Section 1. The $< 10 \text{ K}$ cryogenic environment of CSR facilitates the technical implementation of the large-area micro-calorimeter. The MMC energy resolution demonstrated here will be sufficient to efficiently detect and assign neutral products for DR of molecular ions stored in CSR. We expect achieve mass resolutions of 1 u for neutral DR products from parent molecular ions of mass $\sim 100 \text{ u}$ and perhaps even heavier. The planned detector segmentation approach will allow for differentiation of the various DR fragments and their corresponding masses, thereby enabling the assignment

of the various DR fragmentation channels (see Equation 3) [86, 87]. Moreover, the position sensitivity connected with the detector segmentation will give us a measure on the kinetic energy released in the DR reaction for the various fragmentation channels. As a result, we will also be able to study the internal excitation of the product atoms and molecules can be investigated [88].

The micro-calorimeter detector, in combination with the CSR facility, will be a powerful tool for detailed studies of electron-capture reactions leading to neutral products (such as DR and ECD) in unprecedented detail, particularly for complex molecules. Moreover, we propose to extend molecular ion studies using micro-calorimeters to other reactions yielding neutral products, such as photodissociation, dissociative photodetachment, and collision-induced dissociation. While experimental techniques for studying some of these reactions exist (e.g., [89, 90, 91]), they are usually unable to reliably distinguish and mass-assign multiple neutral fragments. The use of a segmented kinetic-energy-sensitive micro-calorimeter can overcome these limitations also for multi-channel fragmentation reactions involving complex molecular ions, including species of biochemical interest.

Acknowledgments

We acknowledge financial support by the Max-Planck-Society. We thank the MPIK accelerator crew for their excellent support. O.N. and D.W.S. were supported in part by the NSF Division of Astronomical Sciences Astronomy and Astrophysics Grants program and by the NASA Astronomy and Physics Research and Analysis Program. The detector development at Heidelberg University was in part financed through the BMBF grant 05P12VHFA5. D.S. acknowledges the support of the Weizmann Institute of Science through the Joseph Meyerhoff program. The work is supported in part by the German-Israeli Foundation for Scientific Research (GIF under contract no. I-900-231.7/2005). We thank Thomas Stöhlker and collaborators for letting us use indispensable cryogenic equipment during our measurements.

References

- [1] Aebersold R and Mann M 2003 *Nature* **422** 198–207
- [2] Gstaiger M and Aebersold R 2009 *Nature Reviews Genetics* **10** 617–627
- [3] Sturm S, Köhler F, Zatorski J, Wagner A, Harman Z, Werth G, Quint W, Keitel C H and Blaum K 2014 *Nature* **506** 467–470
- [4] de Gouw J and Warneke C 2007 *Mass Spectrometry Reviews* **26** 223–257
- [5] Niemann H B, Atreya S K, Bauer S J, Carignan G R, Demick J E, Frost R L, Gautier D, Haberman J A, Harpold D N, Hunten D M, Israel G, Lunine J I, Kasprzak W T, Owen T C, Paulkovich M, Raulin F, Raaen E and Way S H 2005 *Nature* **438** 779–784
- [6] Li W X, Lundberg J, Dickin A P, Ford D C, Schwarcz H P, McNutt R and Williams D 1989 *Letters to Nature* **339** 534–536
- [7] Rossi D T and Sinz M 2001 *Mass Spectrometry in Drug Discovery* (CRC Press)
- [8] Gross J H 2011 *Mass Spectrometry: A Textbook* (Springer Science & Business Media)
- [9] Wesdemiotis C and McLafferty F W 1987 *Chemical Reviews* **87** 485–500

- [10] Fenn J B, Mann M, Meng C K, Wong S F and Whitehouse C M 1989 *Science* **246** 64–71
- [11] Mann M, Hendrickson R C and Pandey A 2001 *Annual Review of Biochemistry* **70** 437–473
- [12] Sharon M 2010 *Journal of the American Society for Mass Spectrometry* **21** 487–500
- [13] Steen H, Jebanathirajah J A, Rush J, Morrice N and Kirschner M W 2006 *Molecular & Cellular Proteomics* **5** 172–181
- [14] Leo W R 1994 *Techniques for Nuclear or Particle Experiments*. (Springer)
- [15] Chabot M, Della Negra S, Lavergne L, Martinet G, Wohrer-Béroff K, Sellem R, Daniel R, Le Bris J, Lalu G, Gardes D, Scarpaci J A, Désesquelle P and Lima V 2002 *Nuclear Instruments and Methods in Physics Research Section B: Beam Interactions with Materials and Atoms* **197** 155–164
- [16] Abdoul-Carime H, Berthias F, Farizon B and Farizon M 2014 *International Journal of Mass Spectrometry* **365–366** 311–315
- [17] Florescu-Mitchell A and Mitchell J 2006 *Physics Reports* **430** 277–374
- [18] Zubarev R A, Kelleher N L and McLafferty F W 1998 *Journal of the American Chemical Society* **120** 3265–3266
- [19] Syrstad E A and Tureček F 2005 *Journal of the American Society for Mass Spectrometry* **16** 208–224
- [20] Phaneuf R A, Havener C C, Dunn G H and Mller A 1999 *Reports on Progress in Physics* **62** 1143
- [21] Larsson M 1997 *Annual Review of Physical Chemistry* **48** 151–179
- [22] Al-Khalili A, Rosén S, Danared H, Derkach A, Källberg A, Larsson M, Le Padellec A, Neau A, Semaniak J, Thomas R, af Ugglas M, Vikor L, Zong W, van der Zande W, Urbain X, Jensen M, Bilodeau R, Heber O, Pedersen H, Safvan C, Andersen L, Lange M, Levin J, Gwinner G, Knoll L, Scheffel M, Schwalm D, Wester R, Zajfman D and Wolf A 2003 *Physical Review A* **68** 042702
- [23] Wolf A, Buhr H and Novotný O 2011 *Journal of Physics: Conference Series* **300** 012008
- [24] Novotný O, Berg M, Bing D, Buhr H, Geppert W, Grieser M, Grussie F, Krantz C, Mendes M B, Nordhorn C, Repnow R, Schwalm D, Yang B, Wolf A and Savin D W 2014 *The Astrophysical Journal* **792** 132
- [25] Buhr H, Mendes M B, Novotný O, Schwalm D, Berg M H, Bing D, Heber O, Krantz C, Orlov D A, Rappaport M L, Sorg T, Stützel J, Varju J, Wolf A and Zajfman D 2010 *Physical Review A* **81** 062702
- [26] Steinbauer E, Bauer P, Geretschläger M, Bortels G, Biersack J and Burger P 1994 *Nuclear Instruments and Methods in Physics Research Section B: Beam Interactions with Materials and Atoms* **85** 642–649
- [27] Vigren E, Hamberg M, Zhaunerchyk V, Kaminska M, Thomas R D, Trippel S, Wester R, Zhang M, Kashperka I, Ugglas M a, Semaniak J, Larsson M and Geppert W D 2010 *The Astrophysical Journal* **722** 847
- [28] Andersen L H, Heber O and Zajfman D 2004 *J. Phys. B: At. Mol. Opt. Phys.* **37** R57–R88
- [29] Lange M, Froese M, Menk S, Varju J, Bastert R, Blaum K, Lopez-Urrutia J R C, Fellenberger F, Grieser M, von Hahn R, Heber O, Kühnel K U, Laux F, Orlov D A, Rappaport M L, Repnow R, Schröter C D, Schwalm D, Shornikov A, Sieber T, Toker Y, Ullrich J, Wolf A and Zajfman D 2010 *Review of Scientific Instruments* **81** 055105–055105–10
- [30] Thomas R D, Schmidt H T, Andler G, Björkhage M, Blom M, Brnnholm L, Bäckström E, Danared H, Das S, Haag N, Halldén P, Hellberg F, Holm A I S, Johansson H a B, Källberg A, Kälersjö G, Larsson M, Leontein S, Liljeby L, Löfgren P, Malm B, Mannervik S, Masuda M, Misra D, Orbán A, Paál A, Reinhed P, Rensfelt K G, Rosén S, Schmidt K, Seitz F, Simonsson A, Weimer J, Zettergren H and Cederquist H 2011 *Review of Scientific Instruments* **82** 065112
- [31] Nakano Y, Morimoto W, Majima T, Matsumoto J, Tanuma H, Shiromaru H and Azuma T 2012 *Journal of Physics: Conference Series* **388** 142027
- [32] Schmidt H T, Thomas R D, Gatchell M, Rosén S, Reinhed P, Löfgren P, Brännholm L, Blom M, Björkhage M, Bäckström E, Alexander J D, Leontein S, Hanstorp D, Zettergren H, Liljeby L, Källberg A, Simonsson A, Hellberg F, Mannervik S, Larsson M, Geppert W D, Rensfelt K G,

- Danared H, Paál A, Masuda M, Halldén P, Andler G, Stockett M H, Chen T, Källersjö G, Weimer J, Hansen K, Hartman H and Cederquist H 2013 *Review of Scientific Instruments* **84** 055115
- [33] von Hahn R, Berg F, Blaum K, Crespo Lopez-Urrutia J, Fellenberger F, Froese M, Grieser M, Krantz C, Kühnel K U, Lange M, Menk S, Laux F, Orlov D, Repnow R, Schröter C, Shornikov A, Sieber T, Ullrich J, Wolf A, Rappaport M and Zajfman D 2011 *Nuclear Instruments and Methods in Physics Research Section B: Beam Interactions with Materials and Atoms* **269** 2871–2874
- [34] Krantz C, Berg F, Blaum K, Fellenberger F, Froese M, Grieser M, Hahn R v, Lange M, Laux F, Menk S, Repnow R, Shornikov A and Wolf A 2011 *Journal of Physics: Conference Series* **300** 012010
- [35] Enss C 2005 *Cryogenic Particle Detection* 1st ed (Springer Berlin Heidelberg)
- [36] F Simon 1935 *Nature* **135** p763
- [37] Cabrera B, Krauss L and Wilczek F 1985 *Physical Review Letters* **55** 25–28
- [38] Twerenbold D 1986 *Europhysics Letters* **1** 209
- [39] Twerenbold D 1996 *Nuclear Instruments and Methods in Physics Research Section A: Accelerators, Spectrometers, Detectors and Associated Equipment* **370** 253–255
- [40] Hilton G C, Martinis J M, Wollman D A, Irwin K D, Dulcie L L, Gerber D, Gillevet P M and Twerenbold D 1998 *Nature* **391** 672–675
- [41] Frank M, Mears C A, Labov S E, Benner W H, Horn D, Jaklevic J M and Barfknecht A T 1996 *Rapid Communications in Mass Spectrometry* **10** 1946–1950
- [42] Westmacott G, Zhong F, Frank M, Friedrich S, Labov S E and Benner W H 2000 *Rapid Communications in Mass Spectrometry* **14** 600–607
- [43] Suzuki K, Miki S, Shiki S, Zen N, Wang Z and Ohkubo M 2009 *Physica C: Superconductivity* **469** 1677–1679
- [44] Ohkubo M, Shiki S, Ukibe M, Tomita S and Hayakawa S 2011 *International Journal of Mass Spectrometry* **299** 94–101
- [45] Porst J P, Bandler S R, Adams J S, Balvin M A, Busch S E, Eckart M E, Kelley R L, Kilbourne C A, Lee S J, Nagler P C, Porter F S, Sadleir J E, Seidel G M, Smith S J and Stevenson T R 2014 *Journal of Low Temperature Physics* **176** 617–623
- [46] Egelhof P and Kraft-Bermuth S 2005 Heavy ion physics *Cryogenic Particle Detection (Topics in Applied Physics* no 99) ed Enss C (Springer Berlin Heidelberg) pp 469–500
- [47] Horansky R D, Stiehl G M, Beall J A, Irwin K D, Plionis A A, Rabin M W and Ullom J N 2010 *Journal of Applied Physics* **107** 044512–044512–9
- [48] Ranitzsch P, Kempf S, Pabinger A, Pies C, Porst J P, Schäfer S, Fleischmann A, Gastaldo L, Enss C, Jang Y, Kim I, Kim M, Kim Y, Lee J, Lee K, Lee M, Lee S, Yoon W and Yuryev Y 2011 *Nuclear Instruments and Methods in Physics Research Section A: Accelerators, Spectrometers, Detectors and Associated Equipment* **652** 299–301
- [49] Yoo W, Jan Y, Ki G, Ki K, Ki M, Le J, Le K, Le M, Le S, Le H, Yurye Y and Kim Y 2012 *Journal of Low Temperature Physics* **167** 280–285
- [50] Tomita S, Sato Y, Ohkubo M, Ukibe M and Hayakawa S 2007 *Applied Physics Letters* **91** 053507–053507–3
- [51] Ohkubo M, Shigetomo S, Ukibe M, Fujii G and Matsubayashi N 2014 *IEEE Transactions on Applied Superconductivity* **24** 1–8
- [52] Andersen H H 1986 *Nuclear Instruments and Methods in Physics Research Section B: Beam Interactions with Materials and Atoms* **15** 722–728
- [53] Enss C, Fleischmann A, Horst K, Schönefeld J, Sollner J, Adams J S, Huang Y H, Kim Y H and Seidel G M 2000 *Journal of Low Temperature Physics* **121** 137–176
- [54] Fleischmann A, Enss C and Seidel G M 2005 Metallic magnetic calorimeters *Cryogenic Particle Detection (Topics in Applied Physics* no 99) ed Enss C (Springer Berlin Heidelberg) pp 151–216
- [55] Fleischmann A, Gastaldo L, Kempf S, Kirsch A, Pabinger A, Pies C, Porst J P, Ranitzsch P, Schäfer S, Seggern F v, Wolf T, Enss C and Seidel G M 2009 Metallic magnetic calorimeters

- AIP Conference Proceedings* vol 1185 (AIP Publishing) pp 571–578
- [56] Fleischmann A *et al.*, in preparation
 - [57] Pies C, Schäfer S, Heuser S, Kempf S, Pabinger A, Porst J P, Ranitsch P, Foerster N, Hengstler D, Kampkötter A, Wolf T, Gastaldo L, Fleischmann A and Enss C 2012 *Journal of Low Temperature Physics* **167** 269–279
 - [58] Ziegler J F, Ziegler M D and Biersack J P 2010 *Nuclear Instruments and Methods in Physics Research Section B: Beam Interactions with Materials and Atoms* **268** 1818–1823
 - [59] Pies C, Pabinger A, Kempf S, Fleischmann A, Gastaldo L and Enss C 2009 Metallic magnetic calorimeters for high precision QED tests at GSI/FAIR *AIP Conference Proceedings* vol 1185 (AIP Publishing) pp 603–606
 - [60] Szymkowiak A E, Kelley R L, Moseley S H and Stahle C K 1993 *Journal of Low Temperature Physics* **93** 281–285
 - [61] Fleischmann A, Daniyarov T, Rotzinger H, Linck M, Enss C and Seidel G M 2003 *Review of Scientific Instruments* **74** 3947–3954
 - [62] Helmer R G and van der Leun C 2000 *Nuclear Instruments and Methods in Physics Research Section A: Accelerators, Spectrometers, Detectors and Associated Equipment* **450** 35–70
 - [63] Keller M 2014 Bachelor thesis Universität Heidelberg
 - [64] Bortels G and Collaers P 1987 *International Journal of Radiation Applications and Instrumentation. Part A. Applied Radiation and Isotopes* **38** 831–837
 - [65] Kittel C 1976 *Introduction to Solid State Physics* 5th ed (John Wiley & Sons, Inc.)
 - [66] Veje E 1982 *Nuclear Instruments and Methods in Physics Research* **194** 433–436
 - [67] Lörinčík J, Šroubek Z, Eder H, Aumayr F and Winter H 2000 *Physical Review B* **62** 16116–16125
 - [68] Hasselkamp D, Hippler S and Scharmann A 1986 *Nuclear Instruments and Methods in Physics Research Section B: Beam Interactions with Materials and Atoms* **18** 561–565
 - [69] Broeders C H M and Konobeyev A Y 2004 *Journal of Nuclear Materials* **328** 197–214
 - [70] Hildenbrand D L and Hall W F 1962 *The Journal of Physical Chemistry* **66** 754–755
 - [71] Bauer R, Maysenhölder W and Seeger A 1982 *Physics Letters A* **90** 55–58
 - [72] Wales D J and Uppenbrink J 1994 *Physical Review B* **50** 12342–12361
 - [73] Cosulich E, Gatti F and Vitale S 1993 *Journal of Low Temperature Physics* **93** 263–268
 - [74] Porst J P, Höhn C, Haug D, Weldle R, Seidel G M, Gastaldo L, Fleischmann A and Enss C 2008 *Journal of Low Temperature Physics* **151** 436–442
 - [75] Weldle R 2008 *Untersuchung des Effekts magnetischer Verunreinigungen auf das Thermalisierungsverhalten von supraleitenden Teilchenabsorbern* Master thesis Universität Heidelberg <http://www.kip.uni-heidelberg.de/Veroeffentlichungen/details.php?id=1855>
 - [76] Porst J P 2010 *High-Resolution Metallic Magnetic Calorimeters for beta-Spectroscopy on 187-Rhenium and Position Resolved X-Ray Spectroscopy* Dissertation Universität Heidelberg <http://archiv.ub.uni-heidelberg.de/volltextserver/11603/>
 - [77] Powis I and Danby C J 1979 *International Journal of Mass Spectrometry and Ion Physics* **32** 27–33
 - [78] Martinez R I, Ganguli B and Cooks R G 1989 *Rapid Communications in Mass Spectrometry* **3** 427–431
 - [79] Shukla A K, Qian K, Howard S L, Anderson S G, Sohlberg K W and Futrell J H 1989 *International Journal of Mass Spectrometry and Ion Processes* **92** 147–169
 - [80] Martinez R I and Ganguli B 1992 *Journal of the American Society for Mass Spectrometry* **3** 427–444
 - [81] Zhao R, Tosh R, Shukla A and Futrell J 1997 *International Journal of Mass Spectrometry and Ion Processes* **167-168** 317–333
 - [82] O’Hanlon J F 2003 *A User’s Guide to Vacuum Technology* 3rd ed (Hoboken, NJ: Wiley-Interscience)
 - [83] Kampkötter A 2010 *Design-Studie und Entwicklung eines großflächigen metallisch magnetischen Kalorimeters zur orts- und energieauflösenden Detektion*

- von hochenergetischen Molekülfragmenten Master thesis Universität Heidelberg <http://www.kip.uni-heidelberg.de/Veroeffentlichungen/details.php?id=2673>
- [84] Gamer L 2013 *Ein grossflächiges magnetisches Kalorimeter zur energie- und ortsauflösenden Detektion von Molekülfragmenten* Master thesis Universität Heidelberg <http://www.kip.uni-heidelberg.de/Veroeffentlichungen/details.php?id=3116>
- [85] Schulz D 2015 Master thesis Universität Heidelberg
- [86] Buhr H, Mendes M B, O N, Schwalm D, Berg M H, Bing D, Heber O, Krantz C, Orlov D A, Rappaport M L, Sorg T, Stützel J, Varju J, Wolf A and Zajfman D 2010 *Physical Review A* **81** 062702
- [87] Novotný O, Buhr H, Stützel J, Mendes M B, Berg M H, Bing D, Froese M, Grieser M, Heber O, Jordon-Thaden B, Krantz C, Lange M, Lestinsky M, Novotny S, Menk S, Orlov D A, Petrignani A, Rappaport M L, Shornikov A, Schwalm D, Zajfman D and Wolf A 2010 *The Journal of Physical Chemistry A* **114** 4870–4874
- [88] Zajfman D, Amitay Z, Broude C, Forck P, Seidel B, Grieser M, Habs D, Schwalm D and Wolf A 1995 *Physical Review Letters* **75** 814–817
- [89] Lepère V, Lucas B, Barat M, Fayeton J A, Picard V J, Jouvet C, Carcabal P, Nielsen I, Dedonder-Lardeux C, Grégoire G and Fujii A *The Journal of Chemical Physics* **127** 134313
- [90] Pedersen H, Altevogt S, Jordon-Thaden B, Heber O, Rappaport M, Schwalm D, Ullrich J, Zajfman D, Treusch R, Guerassimova N, Martins M, Hoeft J T, Wellhöfer M and Wolf A 2007 *Physical Review Letters* **98** 223202
- [91] Poad B L J, Ray A W and Continetti R E 2013 *The Journal of Physical Chemistry A* **117** 12035–12041

